Journal of Materials Chemistry A

Iron(III) oxyhydroxide and oxide monoliths with controlled multiscale porosity: synthesis and their adsorption performance

Journal:	*Journal of Materials Chemistry A*
Manuscript ID	TA-ART-02-2018-001691.R1
Article Type:	Paper
Date Submitted by the Author:	05-Apr-2018

Complete List of Authors:	Hara, Yosuke; Kyoto University, Graduate School of Science, Dept. of Chemistry Kanamori, Kazuyoshi; Kyoto University, Department of Chemistry, Graduate School of Science Morisato, Kei; GL Sciences Inc., Miyamoto, Riichi; Kyoto University, Chemistry Nakanishi, Kazuki; Kyoto University, Graduate School of Science, Dept. of Chemistry

Journal Name

ARTICLE

Iron(III) oxyhydroxide and oxide monoliths with controlled multiscale porosity: synthesis and their adsorption performance

Yosuke Hara,[a] Kazuyoshi Kanamori, [a] Kei Morisato, [a,b] Riichi Miyamoto,[a,c] and Kazuki Nakanishi [a]*

Received 00th January 20xx,
Accepted 00th January 20xx

DOI: 10.1039/x0xx00000x

www.rsc.org/

Iron(III) oxyhydroxide and oxide monoliths with controlled multiscale porosity have been successfully fabricated via the sol-gel process accompanied by phase separation. The size of macropores was controlled by synthetic parameters such as starting compositions. The as-dried iron(III) oxyhydroxide monoliths were amorphous and possessed surface area over 340 m^2 g^{-1}, of which mesostructures could be further controlled by a heat-treatment at 250-350 ˚C without collapse of macrostructures and monolithic forms. When the as-dried gel was heated at 300 ˚C, the resultant gel transformed to crystalline α-Fe_2O_3 and exhibited the specific surface area of 124 m^2 g^{-1}. The heat-treatment at 350 ˚C resulted in the broadened size distribution of mesopores. Adsorption behavior of the Congo red has revealed that the interconnected macroporous structure contributed to faster diffusion and better accessibility in a continuous flow-through set up, and the crack-free monolithic forms accounted for an advantageous use of the flow-through adsorbents.

1. INTRODUCTION

Over the past decades, research activities on hierarchically porous materials have achieved remarkable progress in various application areas such as catalysis, separation, adsorption, energy storage and conversion, life sciences, and other industrial applications.[1-3] Porous structures over multiple length-scales offer better functionalities in materials depending on the combination of the discrete pore structures, e.g. micro- (<2 nm) and mesopores (2-50 nm) provide the size and shape selectivity and impart high surface areas, while macropores (>50 nm) enhance the diffusion and accessibility to the active sites.[4] To design such hierarchically structured materials, it is essential to control various properties such as pore sizes and size distributions, surface areas, chemical compositions and crystallinity.

One strategy to control the multiscale porous structures is the sol-gel process accompanied by phase separation. [5] Most of this approach is based on the polymerization-induced phase separation, in which the polymerization reaction and the phase separation occur simultaneously, and the transient structure of the phase separation is frozen by the sol-gel transition. As a result, monolithic materials with well-defined interconnected macropores and mesostructured skeletons can be obtained.[4,5] Their structural properties, which give higher diffusivity and better accessibility, and lower back pressure are advantageous as separation media[6], catalysts[7], catalyst supports[8-9], and adsorbents.[10] Meanwhile, the reactivity of the precursor and the behaviour of polymerization have a strong influence on the phase separation and the gelation, it is therefore necessary to find suitable synthesis conditions for each specific composition.

In 2007, Tokudome et al. reported hierarchically structured Al_2O_3 monoliths prepared by combining phase separation and the epoxide-mediated sol-gel process.[11,12] Extending this synthetic approach, similar hierarchically structured monoliths of mixed metal oxide[13-15] and tri-modal pore structured zeolite monoliths[16] were also reported. In addition, several attempts have been made to extend the above approach to other metal-based monolithic materials.[17-20] For example, Kido et al. reported iron-based monoliths by combining phase separation and the epoxide-mediated sol-gel process.[17] According to their report, compared to the previous work, the main difficulty in obtaining iron(III) oxyhydroxide-based monoliths lies in the strong tendency of the precursor sol to form precipitates of iron(III) oxyhydroxide in the aqueous solution. In order to circumvent this problem, poly(acrylamide) was added as a precipitation inhibitor and a phase separation inducing argent. The -OH groups of iron(III) oxyhydroxide interact with amide groups of poly(acrylamide) via strong hydrogen bond, and the complexes of them exhibit relatively hydrophobic character, which leads to macroscopic phase separation in the aqueous solution. This approach could be applied to other metal (oxy)hydroxide-based monolithic materials[18,19,20] and has usefulness that the obtained wet gels can be easily dried without collapsing monolithic forms because of the organic polymer distributed in the skeleton. While having such advantages, however, the obtained as-dried gels contain a large

[a] Department of Chemistry, Graduate School of Science, Kyoto University, Kitashirakawa, Sakyo-ku, Kyoto 606-8502, Japan.
E-mail: Kazuki@kuchem.kyoto-u.ac.jp
[b] GL Sciences, Inc. 237-2 Sayamagahara, Iruma, Saitama, 358-0032, Japan.
[c] SnG Inc., 1-39 Goryo-Ohara, Nishikyo-ku, Kyoto 615-8245, Japan.

† Electronic Supplementary Information (ESI) available: the molecular structure of Congo red; time evolutions of pH in the reaction solution; mesopore size distributions of the as-dried monoliths with varied starting compositions; change in diameter of the monoliths during gelation, drying, and heat treatment processes; macropore size distributions of the monoliths heat treated at different temperatures; UV-Vis adsorption spectra of Congo red solutions treated by different samples; SEM images of the crushed monoliths. See DOI: 10.1039/x0xx00000x

amount of organic polymer in the skeletons, and calcination under air causes serious damage of macro-morphology and collapse of the monolithic forms. It is therefore difficult to obtain pure metal (oxy)hydroxide and oxide monoliths with well-defined macropores and a crack-free monolithic form by this synthetic approach. Macro-morphology and the monolithic forms can be preserved by calcination in an inert condition, which leaves a large amount of carbon in the obtained gels. While the carbon in the skeletons can be activated to offer abundant micropores, it cannot be removed without damage on the monoliths to obtain carbon-free metal (oxy)hydroxides and oxides. For these reasons, from the viewpoint of controlling hierarchically porous structures of metal (oxy)hydroxides and oxides monoliths, alternative approaches are needed to prepare monoliths in which excessive organic polymer is not distributed in the skeletons. In this report, we focus on iron(III) oxyhydroxide and oxide monoliths.

Porous iron(III) oxyhydroxide and oxide are used in various fields. For example, they are used as adsorbents for water treatment to remove, for example, Cr(VI), As(V), and organic pollutants.[21-27] In particular, α-Fe_2O_3, the most stable phase of iron oxides, has been extensively used as catalysts[28,29], catalyst supports[30,31], and separation media[32]. In those various applications, for example as adsorbents for water treatment, adsorption sites on the surface and the accessibility to them are important factors.[23] In addition, crystallinity and surface properties are also important as catalysts and catalyst supports.[28-31] As separation media, high surface area, high macropososity, and a suitable mesopore size distribution are required to achieve fast and efficient separation.[32] Thus, when considering such applications, it is highly important to design materials with controllable properties for each specific application. In this study, we have synthesized hierarchically porous iron(III) oxyhydroxide and oxide monoliths by a novel approach, and controlled the multiscale structures without collapse of macrostructure and monolithic forms. Moreover, the influence of the hierarchical structures on their adsorption performance is also discussed.

2. MATERIALS AND METHODS

2.1. Chemicals

Poly(ethylene oxide) (PEO, ≥96 %, M_n = 1,000,000 Da), iron(III) chloride hexahydrate $FeCl_3 \cdot 6H_2O$ (≥97 %), propylene oxide (≥99 %), and Congo red were purchased from Sigma-Aldrich Co. (USA). *N*,*N*-dimethylformamide (DMF, ≥99.5 %), 2-propanol (≥99.5 %), and *n*-hexane (≥99.5 %) were purchased from Kishida Chemical Co., Ltd. (Japan). Na_2CO_3 (≥99.5%) and $NaNO_3$ (≥99.5%) were purchased from Hayashi Pure Chemical Ind. Ltd. (Japan). All reagents were used as received. Distilled water was used in all experiments.

2.2. Preparation of iron(III) oxyhydroxide and oxide monoliths

The typical iron(III) oxyhydroxide monoliths and α- Fe_2O_3 monoliths were synthesized by the following procedure. A given amount of PEO (w_{PEO}) was completely dissolved in 8.0 mL of DMF at 80 °C in a glass bottle, and then the solution was cooled down to room temperature (25 °C). The 3.20 g of $FeCl_3 \cdot 6H_2O$ (11.8 mmol) was subsequently added to obtain a homogeneous solution. After stirring for 10 min at room temperature, 4.0 mL of propylene oxide ([propylene oxide]/[Fe] ~ 4.8 in molar ratio) was added and stirred for 1 min, and then the solution was transferred into a glass tube. The tube was sealed and kept at 40 °C for gelation. After gelation, the wet gels were kept for at 40 °C for 1 h, and then kept at 80 °C for 24 h for aging. The obtained wet gels were washed with 2-propanol at 60 °C for 12 h twice, and with *n*-hexane at 40 °C for 12 h twice, and then finally dried at 40 °C in 110 mL glass bottles with a cap, which had a 2-mm hole. Xerogels thus obtained were completely dried at 120 °C. Some of the as-dried gels were heat-treated at various temperatures between 250 °C and 350 °C. The temperature was raised from 120 °C to the target temperature with a heating rate of 0.4 °C min^{-1} and the samples were held at the temperature for 6 h.

2.3. Characterization

The time evolution of solution pH was monitored at 40 °C using a pH meter (F-21, Horiba, Ltd., Japan). Microstructures of the fractured surfaces of the samples were observed using a scanning electron microscope (SEM: JSM-6060S, JEOL, Japan), a field emission scanning electron microscope (FE-SEM: JSM-6700F, JEOL, Japan). Macropore size distributions were measured by mercury porosimetry (Autopore IV 9505, Shimadzu Co., Japan). The thermal properties of the samples were investigated by thermogravimetry-differential thermal analysis (TG-DTA: Thermo plus EVO2 TG 8120, Rigaku Co., Japan) with a continuous air supply at 100 mL min^{-1}. The crystal structure was examined by powder X-ray diffraction (XRD: RINT Ultima III, Rigaku Co., Japan) using Cu Kα (λ = 0.154 nm) as an incident beam. Micro-/mesostructure of the samples were characterized by nitrogen adsorption-desorption (BELSORP-mini II, Bel Japan Inc., Japan). Helium pycnometry (Ultrapyc 1200e, Quantachrome Instruments, USA) was employed to determine the skeletal density.

2.4. Adsorption measurement

The adsorption performance of the synthesized iron(III) oxyhydroxide and oxide monoliths has been examined by removal of dyes in aqueous solution. Congo red, sodium salt of 3,3′-([1,1′-biphenyl]-4,4′-diyl)bis(4-aminonaphthalene-1-sulfonic acid) (Fig. S1), was selected as a model adsorbate. To examine the influences of micro-/mesoporous structures on their adsorption capacity, 2.0 to 36.0 mg of crushed monoliths (< 20 μm) were immersed in with 20 mL of 100 mg L^{-1} aqueous solution of Congo red. After stirring for 72 h, the aqueous supernatant phase was extracted, and the absorbance spectra of the supernatant solution were obtained by a UV-Vis spectrophotometer (V-670, JASCO, Japan). The residual concentrations of Congo red were obtained by using a calibration curve over 5-80 mg L^{-1} in the wavelength range of 400-600 nm. The maximum adsorption capacities of the monoliths were calculated assuming that Congo red other than

that remaining in the solution were adsorbed to the adsorbents. The zeta potentials were measured using a Malvern Zetasizer 1000 (Malvern, England). In this measurement, 4.0 mg of the crushed monoliths (<20 μm) were immersed in with 20 mL of 0.010 mol L^{-1} $NaNO_3$ aqueous solutions. After sonicated for 10 min, the suspensions were stood still at room temperature for 24 h to stabilize the ionic strength during the measurement. Then, the supernatants of the suspensions were used for the zeta potential measurements. The influences of macroscopic forms and interconnected macroporous structures on their adsorption performance were examined in a flow-through set up. The macroporous monolith, crushed macroporous monoliths (45-100 μm) and non-macroporous crushed monoliths (45-100 μm) were used as adsorbents. The 160 mL of 100 mg L^{-1} aqueous Congo red solution were pumped into the packed beds of the adsorbents using a syringe pump at room temperature. (Regarding the monolith, the aqueous Congo red solution was pumped after conditioning the surface with H_2O.) The removal efficiency of Congo red was examined by analyzing the absorbance spectra of the eluted solutions with the increment of 20 mL. The pH of the obtained solutions of adsorption measurement was adjusted to be ca. around 7 by 5 mg of Na_2CO_3 powder. The leakage of the adsorbent was characterized by measuring iron concentration of the treated solutions by inductively coupled plasma atomic emission spectroscopy (ICP-AES: Varian 720-ES, Agilent Technology Inc., USA). Before the measurement, the solution was filtered through a membrane with 0.22 μm openings.

3. RESULTS AND DISSCUSSION

3.1 Formation and control of interconnected macropores

In this work, we introduced a novel synthetic approach, which is different from the previous work[17], to prepare the monoliths in which excessive organic polymer is not included in the gel skeletons. We adopted PEO, which has a weak interaction with iron(III)-containing species, as a phase separation inducing agent. The suitable starting compositions and reaction conditions have been specified in which iron(III) oxyhydroxide and PEO are distributed as the major components respectively to the gel- and solvent-phases as a result of phase separation.

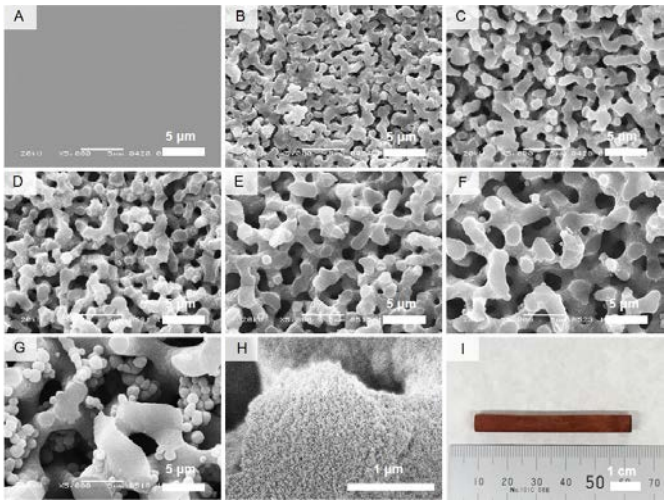

Figure 1. (A-G) SEM images of the as-dried iron(III) oxyhydroxide monoliths prepared with varied amounts of PEO: w_{PEO} = (A) 30 mg (B) 35 mg (C) 40 mg (D) 45 mg (E) 50 mg (F) 55 mg (G) 60 mg. (H) FE-SEM image of the as-dried iron(III) oxyhydroxide monolith: w_{PEO} = 50 mg. (I) Appearance of the as-dried iron(III) oxyhydroxide monolith: w_{PEO} = 50 mg.

The morphology of interconnected macroporous structures could be controlled by changing the starting composition (Scheme 1). The PEO amount was used as a variable. As Gash and co-workers have previously shown[11], gelation of metal salt solution is induced using epoxides as an acid scavenger, which causes the solution pH to increase, and then iron(III) oxyhydroxide-based gels are formed[33]. We adopted DMF, which strongly solvate to metal ions[34], as the main solvent. Thus, the excessive heat generation due to polycondensation[11] were prevented. Figure S2 shows the time evolutions of pH of the reaction solution until the sol-gel transition (w_{PEO} = 0 mg). In this case without PEO, a uniform transparent gel is formed in ~15 min. On the other hand, opaque gels are formed when PEO exceeding 35 mg is employed. When the water ratio is high, opaque gels or precipitates formed (w_{PEO} = 0 mg).

Figure 1A-G show the SEM images of as-dried monoliths with varied PEO amounts. Formation and coarsening of the interconnected macroporous structures were seen with an increase of PEO amount. Figure 2 shows the results of mercury intrusion measurements. The obtained parameters of macroporous structure are summarized in Table 1. In the present range of starting composition, it was possible to control the macropore diameter from 0.28 μm to 2.5 μm with the sharp

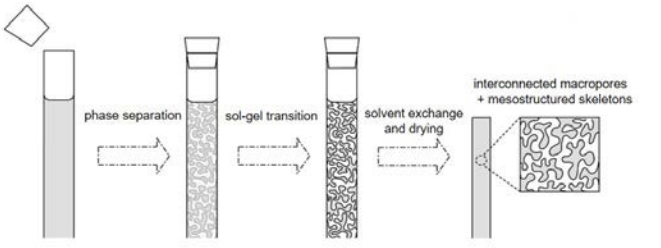

Scheme 1. Schematic representation of preparation of iron(III) oxyhydroxide monoliths.

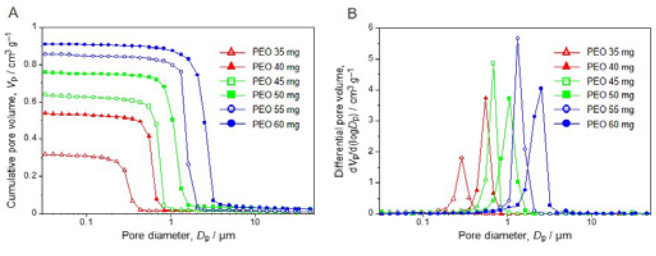

Figure 2. (A) Cumulative and (B) differential pore size distributions of as-dried iron(III) oxyhydroxide monoliths prepared with varied amounts of PEO.

size distribution as summarized in Table 1. Bulk density, skeletal density and porosity are also shown in Table 1. In particular, at w_{PEO} = 60 mg, many spherical particles precipitated on the skeleton surface (Fig. 1G). This is presumably due to the secondary phase separation occurring in the solvent phase after gelation[35]. The mesoscopic structures observed by FE-SEM and the macroscopic appearance of the samples form at w_{PEO} = 50 mg are shown in Fig. 1H and Fig. 1I, respectively. It was confirmed that the obtained as-dried monoliths had hierarchical structures covering from macroporous to mesoporous size regions. The crack-free monolithic samples could be obtained by replacing the pore liquid with *n*-hexane, which has low surface tension and hydrophobicity[36], and subsequent slow ambient pressure drying. Nitrogen adsorption-desorption measurement was carried out to investigate the effect of PEO amount in the mesoscopic region (Fig. S3, Table 1). As a result, only negligible differences were recognized among the samples prepared with varied amounts of PEO in the mesoscopic region.

The phase separation tendency is related to the miscibility of a polymeric system, which can be estimated by the Flory-Huggins formula. [37-39] The Gibbs free energy change of mixing, ΔG is expressed as;

$$\Delta G \propto RT[\{(\phi_1/P_1)\ln \phi_1 + (\phi_2/P_2)\ln \phi_2\} + \{\chi_{12}\phi_1\phi_2\}]$$

Here, φ_i and P_i (i = 1,2) denote the volume fraction and degree of polymerization of component i, respectively, and χ_{12} shows the interaction parameter, and R and T are the gas constant and temperature, respectively. The former two terms in parenthesis represent the entropic contribution, and the last term the enthalpic contribution.

As can be seen from the results of mercury intrusion measurement, the volume fraction of the skeleton decreases as the amount of PEO increases (Fig. 2A). This tendency is opposite to the case of FeOOH-poly(acrylamide) monoliths[17], where the volume fraction of the gel skeleton increased with an increase of added polymer. The TG-DTA measurement showed almost no difference in TG and DTA curves between as-dried monoliths prepared with and without PEO. The above results indicate that it can be considered that PEO and iron(III) oxyhydroxide oligomers are respectively major constituents of solvent- and gel-phase, and PEO can be almost completely removed by the solvent exchange.

3.2 Control of crystallinity and mesostructures

For the obtained as-dried monoliths (w_{PEO} = 50 mg), calcination was carried out, and the results of XRD measurement are shown in Fig. 3B. Although no obvious diffractions were observed for the samples heat-treated at 250 °C, diffractions corresponding to α-Fe_2O_3 (PDF No. 33-0664 from JCPDS-ICDD) appeared in the sample heat-treated at 300 °C. In the sample heat-treated at 350 °C, the intensities and widths of the peaks increased due to the growth of the crystallites. The thermal analysis of the as-dried monoliths showed that the weight loss occurred in the temperature range 200-300 °C (Fig. 3A). From the result of the XRD measurement, the weight loss corresponds to the loss of water generated by the transformation from oxyhydroxide to oxide. Substantial shrinkage was observed on the heat-treatment of the monoliths (Fig. S4), and crack formations were observed depending on the heating rate. The heat-treatment carried out at 0.4 °C min^{-1} as the highest heating rate avoided cracking. Fig. 3C-H show results of SEM and FE-SEM observations, respectively. Here, the entire macroporous structures and the monolithic forms were maintained during the heat-treatment. On the other hand, it was found that the grains constituting the skeleton grew in size as the heat-treatment temperature increased (Fig.3F-H). The mercury intrusion measurements showed that the macropore diameter decreased by 25 % at 250 °C, but remained almost unchanged by further heating from 250 to 350 °C (Fig. S5, Table 1). Nitrogen sorption measurements showed that the mesopore size distribution shifted considerably to larger pore size range with

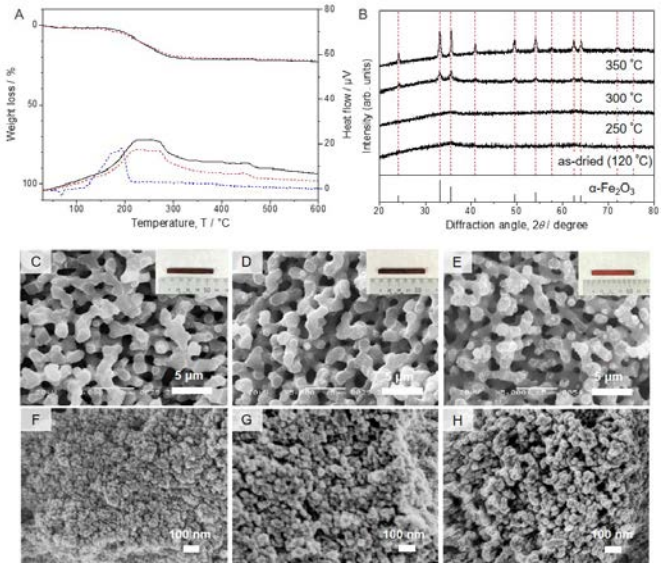

Figure 3. (A)TG curves and DTA curves; as-dried monolith: w_{PEO} = 50 mg (black curves), as-dried monolith: w_{PEO} = 0 mg (red dash curve), and PEO (blue dash curve). (B) XRD patterns of the samples heat-treated at different temperatures. (C-E) SEM images of heat-treated iron(III) oxide monoliths and their appearance; (C) 250 °C (D) 300 °C (E) 350 °C. (F-H) FE-SEM images of heat-treated iron(III) oxide monoliths; (F) 250 °C (G) 300 °C (H) 350 °C.

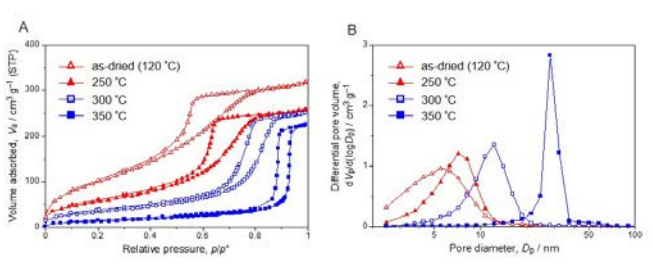

Figure 4. (A) Nitrogen adsorption-desorption isotherms (B) BJH pore size distributions obtained from the adsorption branch of iron(III) oxyhydroxide or oxide monoliths heat treated at different temperatures.

an increase of the heat-treatment temperature (Fig. 4B, Table 1).

3.3 Influences of hierarchical structures on their adsorption performance

Aqueous Congo red solution was selected as a model adsorbate. Congo red is typically adsorbed onto the surface of iron oxides and (oxy)hydroxides by interacting with iron and hydroxide groups of them with the amine groups of Congo red molecules, by coordination and H-bonding, respectively.[27] It is widely used as an adsorption model due to its strong absorbance in the visible region, and the results can be compared with a lot of preceding works.

3.3.1. Influences of micro-/mesoporous structures on their maximum adsorption capacity

Figure S6 shows the absorption spectra of the Congo red solutions after the treatment with crushed monoliths (<20 μm) for 72 h. The initial concentration of the Congo red solution was 100 mg L^{-1}. In Fig. S6a, the Congo red was almost completely removed from the water by 6.0 mg of as-dried iron(III) oxyhydroxide monoliths (w_{PEO} = 50 mg). The maximum adsorption capacities of the monoliths to Congo red estimated from the similar measurements using 2.0 mg and 4.0 mg of the monoliths were 473 mg g^{-1} and 467 mg g^{-1}, respectively. There was almost no difference of the obtained maximum adsorption capacities regardless of the absolute amount of the monoliths between 2.0 mg and 4.0 mg. The maximum adsorption capacity of the as-dried iron(III) oxyhydroxide monoliths is much higher than that of the majority of previously reported iron oxyhydroxide and oxide porous materials.[21-27] Figure S6B shows the absorption spectra of the Congo red solutions after

Table 1. Pore properties of the samples heat-treated at different temperatures.

sample	d_{macro}[a] /μm	d_{meso}[b] /nm	ρ_b[c] /g cm^{-3}	ρ_s[d] /g cm^{-3}	Porosity[e] /%	S_{BET}[f] /m^2 g^{-1}
as-dried (w_{PEO} = 0 mg)	-	5.5	-	-	-	371
as-dried (w_{PEO} = 30 mg)	-	5.5	-	-	-	405
as-dried (w_{PEO} = 35 mg)	0.28	5.5	0.815	2.22	63	340
as-dried (w_{PEO} = 40 mg)	0.55	5.5	0.626	2.22	72	382
as-dried (w_{PEO} = 45 mg)	0.67	4.9	0.573	2.19	74	357
as-dried (w_{PEO} = 50 mg)	1.10	5.5	0.557	2.17	74	384
as-dried (w_{PEO} = 55 mg)	1.30	4.9	0.550	2.04	73	348
as-dried (w_{PEO} = 60 mg)	2.50	5.5	0.462	1.66	72	349
sample heated at 250 °C	0.83	7.2	0.630	2.87	78	212
sample heated at 300 °C	0.83	12.2	0.540	2.65	80	124
sample heated at 350 °C	0.83	28.1	0.647	3.02	79	49

[a] Macropore size determined by the mercury porosimetry. [b] BJH mesopore size determined by the nitrogen sorption analysis. [c] Bulk density obtained by the mercury porosimetry. [d] Skeletal density obtained by helium pycnometry. [e] Calculated by 100 × (1- ρ_b/ρ_s). [f] Specific surface area obtained by the BET method.

Table 2. BET surface area and the maximum Congo red removal capacity of various adsorbents.

Adsorbent Sample	S_{BET} /m^2 g^{-1}	Maximum Adsorption Capacity for Congo red, C_{max} /mg g^{-1}	Reference
as-dried (50): amorphous FeOOH	384	467	this study
as-dried (0): amorphous FeOOH	371	452	this study
sample heated 250 °C : -	212	185	this study
sample heated 300 °C: crystalline α-Fe_2O_3	124	123	this study
sample heated 350 °C : crystalline α-Fe_2O_3	49	64	this study
mesoporous α-Fe_2O_3	111	53	21
hollow urchin-like α-FeOOH nanostructures	239	239	22
hierarchical urchin-like α-Fe_2O_3	69	66	22
hollow nest-like α-Fe_2O_3 sphere	152	160	23
α-Fe_2O_3 hollow structures	33	94	24
α-Fe_2O_3 nanoparticles and nanowhiskers	164	254	25
α-Fe_2O_3 nanorods	23	78	26
α-Fe_2O_3 porous nanorods	23	78	27
α-FeOOH nanorods	39	160	27

treatments using 4.0 mg of crushed monoliths with different macro-mesoporous structures. The maximum adsorption capacities calculated from the obtained spectra are summarized in Table 2, and the adsorption isotherms are shown in Figure S7. The zeta potential and the corresponding pH of the different samples are summarized in Table S1. Only negligible differences in the maximum adsorption capacity and the zeta potential were recognized between monoliths with (w_{PEO} = 50 mg) and without (w_{PEO} = 0 mg) macropores, indicating that the molecular level surface environments are essentially the same regardless of the presence of macropores. With an increase of the heat-treatment temperature, the zeta potential value changed from positive to negative, and the corresponding pH of the solution increased. This is due to the reduction of surface hydroxy groups accompanied by the transformation from oxyhydroxide to oxide. The temperature evolution of BET surface area also indicates the reduction of hydroxyl groups at elevated temperatures. The abundant surface hydroxy groups are therefore considered to contribute to the high values of adsorption capacity[27]. It was not, however, possible to clearly distinguish the effects of hydroxy concentration and zeta potential on the maximum adsorption capacity possibly because those parameters are closely interrelated.

3.3.2. Influences of macroscopic forms and interconnected macroporous structures on their performance as the flow-through adsorbents

The macroporous monolith (w_{PEO} = 50 mg: denoted as *adsorbent a*), crushed macroporous monoliths (w_{PEO} = 50 mg, 45-100 μm: *adsorbent b*), and crushed non-macroporous monoliths (w_{PEO} = 0 mg, 45-100 μm: *adsorbent c*) were used as the adsorbents in the flow-through set up. Scanning electron micrographs of *adsorbent b* and *c* are shown in Fig. S8. The 160 mL of 100 mg L^{-1} Congo red solution was pumped into the packed beds of the 0.10 g of adsorbents (Fig. 5A). Figure 5b shows the appearance of the flow-through adsorbents when 15 mL of the Congo red solution was loaded. Figure 6a shows the removal efficiencies of Congo red with the loading increment of 20 mL. The removal efficiencies were also investigated by normalizing to the column volume of 0.18 cm^3, which was the volume of 0.10 g of *adsorbent a* (Fig. 6B). Here, it was impossible to pump into the non-macroporous monolith (w_{PEO} = 0 mg) because of its high back pressure.

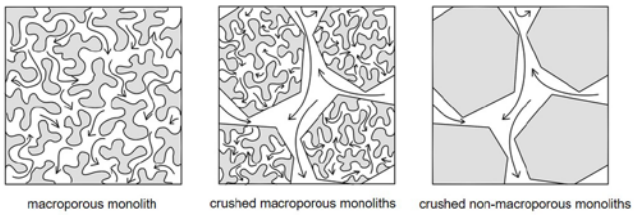

Scheme 2. Schematic illustration of the influences of macroscopic forms (monolith vs. powder) and macroporous structure on mass-transfer.

As shown in Fig. 6AB, the *adsorbent b* and the *adsorbent c* exhibited significant differences in the adsorption performance on both mass and column volume bases. With loading of 20 mL, the removal efficiencies of Congo red were nearly 100 % by the *adsorbent b*, whereas less than 50 % by the *adsorbent c.* The enhanced mass transport by the interconnected macroporous structure into the particles made this difference (Scheme 2). The interconnected macropores strongly influence on the mass transport efficiency and adsorption performance in the flow-through set up for the particles with the similar macroscopic sizes.

The removal efficiency of the *adsorbent b* was higher than that of the *adsorbent a* per mass, whereas the opposite result was obtained per column volume (Fig. 6). Regarding the results per mass, the difference of these removal efficiencies can be due to the larger macroscopic surface area and the larger apparent column volume caused by crushing. It can be considered that the resulting macroscopic surface area contributed to improve the accessibility to the adsorption sites, and larger column volume contributed to higher contact probability of the solution to the adsorbent. When normalized by the column volume, the mass of the *adsorbent a* is about 1.8 times larger than that of the *adsorbent b*, (0.10 g vs. 0.055 g), thus the removal efficiencies of the *adsorbent a* became apparently higher than that of the *adsorbent b* per column volume.

To investigate the stability of the adsorbent, the iron concentration of the total treated solution from *adsorbent a* (0.10 g) was measured by the ICP-AES. The concentration of iron was determined under 0.10 ppm. The result ensures the sufficient stability of the adsorbent in the flow-through set-up.

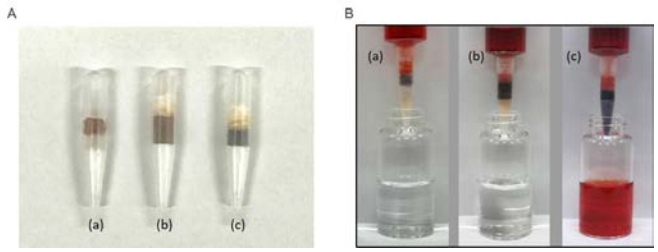

Figure 5. Appearance of the packed beds of the adsorbents. The weight of each adsorbent is fixed as 0.10 g. (B) Appearance of the continuous flow-through adsorbents when pumped with 15 mL of aqueous Congo red solution. (a) As-dried macroporous monolith 0.10 g: w_{PEO} = 50 mg. (b) As-dried crushed macroporous monoliths 0.10 g: w_{PEO} = 50 mg. (c) As-dried crushed non-macroporous monoliths 0.10 g: w_{PEO} = 0 mg.

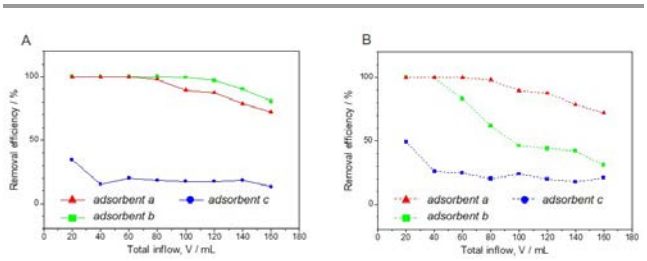

Figure 6. Removal efficiency by each packed bed. The efficiency is normalized by (A) the weight of each adsorbent (0.10 g) and (B) the column volume of each adsorbent (0.18 cm^3). The weights of adsorbent a, b and c in (B) are 0.10 g, 0.055 g and c = 0.11 g, respectively.

From these facts, macroporous monoliths with multiscale porosity can be considered to have high benefits to improve adsorption performance per column volume, and even crushed macroporous monoliths can offer higher performance than the particles of similar size without macropores in the flow-through set up. Depending on the applications, designing hierarchical structures from the meso- and micro- to macroscopic scales is one of the most important strategies to realize better functionalities in inorganic materials. We found that this can be realized in this work, and also aim to establish multiscale porous structures control methods for other transition metal-based materials.

Conclusions

In summary, we have successfully synthesized crack-free iron(III) oxyhydroxide and oxide monoliths with controlled multiscale porosity via a modified sol-gel process accompanied by phase separation. In particular, an employment of a water-soluble polymer PEO that induces phase separation and does not have strong interactions with iron ions and (oxy)hydroxide species leads to macropore skeletons with a higher fraction of inorganic species. The resultant materials are thus mechanically stable enough to reproducibly give crack-free iron(III) oxide monoliths by calcination.

In the flow-through set up, the adsorption performance decreased in the order of macroporous monolith, crushed macroporous monoliths, and crushed non-macroporous monoliths. The interconnected macroporous structures had a great advantage on the mass transport into the particles, and provided better accessibility. In addition, the crack-free macroporous monolith had the highest removal efficiency per column volume because of its higher density and good accessibility. This synthetic strategy to control the multiscale porous structure of iron(III) oxyhydroxide and oxide monoliths can be applied to the other applications in flow-through systems such as catalysis and separation.

Acknowledgements

The authors would like to thank Prof. M. Tafu and Ms. N. Okajima at National Institute of Technology, Toyama College for the ICP-AES analysis. We also thank Prof. T. Sakka, N. Nishi, and Mr. T. Ishihara at Department of Energy and Hydrocarbon Chemistry, Graduate School of Engineering, Kyoto University for their assistance on zeta potential measurements. The present study has been performed under financial supports from Advanced Low Carbon Technology Research and Development Program (ALCA, Japan Science and Technology Agency).

References

1 B.-L. Su, C. Sanchez and X.-Y. Yang, *John Wiley & Sons*, 2012.
2 X. Y. Yang, L. H. Chen, Y. Li, J. C. Rooke, C. Sanchez and B. L. Su, *Chem. Soc. Rev.*, 2017, **46**, 481.
3 M. H. Sun, S. Z. Huang, L. H. Chen, Y. Li, X. Y. Yang, Z. Y. Yuan and B. L. Su, *Chem. Soc. Rev.*, 2016, **45**, 3479.
4 A. Feinle, M. S. Elsaesser and N. Hüsing, *Chem. Soc. Rev.*, 2016, **45**, 3377.
5 K. Nakanishi and N. Tanaka, *Acc. Chem. Res.*, 2007, **40**, 863.
6 A. M. Siouffi, *J. Chromatogr. A.*, 2006, **1109**, 1.
7 A. Sachse, A. Galarneau, F. Di Renzo, F. o. Fajula and B. Coq, *Chem. Mater.*, 2010, **22**, 4123.
8 N. Moitra, A. Matsushima, T. Kamei, K. Kanamori, Y. H. Ikuhara, X. Gao, K. Takeda, Y. Zhu, K. Nakanishi and T. Shimada, *New J. Chem.*, 2014, **38**, 1144.
9 C. H. Pélisson, T. Nakanishi, Y. Zhu, K. Morisato, T. Kamei, A. Maeno, H. Kaji, S. Muroyama, M. Tafu, K. Kanamori, T. Shimada and K. Nakanishi, *ACS Appl. Mater.*, 2017, **9**, 406.
10 Y. Zhu, T. Shimizu, T. Kitajima, K. Morisato, N. Moitra, N. Brun, T. Kiyomura, K. Kanamori, K. Takeda, H. Kurata, M. Tafu and K. Nakanishi, *New J. Chem.*, 2015, **39**, 2444.
11 A. E. Gash, T. M. Tillotson, J. H. Satcher, J. F. Poco, L. W. Hrubesh and R. L. Simpson, *Chem. Mater.*, 2001, **13**, 999.
12 Y. Tokudome, K. Fujita, K. Nakanishi, K. Miura and K. Hirao, *Chem. Mater.*, 2007, **19**, 3393.
13 Y. Tokudome, K. Fujita, K. Nakanishi, K. Kanamori, K. Miura, K. Hirao, T. Hanada, *J. Ceram. Soc. Japan.*, 2007, **115**, 925.
14 Y. Tokudome, N. Tarutani, K. Nakanishi and M. Takahashi, *J. Mater. Chem. A*, 2013, **1**, 7702.
15 K. Fujita, Y. Tokudome, K. Nakanishi, K. Miura and K. Hirao, *J. Non-Cryst. Solids*, 2008, **354**, 659.
16 Y. Tokudome, K. Nakanishi, S. Kosaka, A. Kariya, H. Kaji and T. Hanada, *Micropor. Mesopor. Mater.,* 2010, **132**, 538.
17 Y. Kido, K. Nakanishi, A. Miyasaka and K. Kanamori, *Chem. Mater.*, 2012, **24**, 2071.
18 Y. Kido, G. Hasegawa, K. Kanamori and K. Nakanishi, *J. Mater. Chem. A*, 2014, **2**, 745.
19 Y. Kido, K. Nakanishi, N. Okumura and K. Kanamori, *Micropor. Mesopor. Mater.*, 2013, **176**, 64.
20 S. Fukumoto, K. Nakanishi and K. Kanamori, *New J. Chem.*, 2015, **39**, 6771.
21 C. Yu, X. Dong, L. Guo, J. Li, F. Qin, L. Zhang, J. Shi and D. Yan, *J. Phys. Chem. C*, 2008, **112**, 13378.
22 J. Fei, Y. Cui, J. Zhao, L. Gao, Y. Yang and J. Li, *J. Mater. Chem.*, 2011, **21**, 11742.
23 Z. Wei, R. Xing, X. Zhang, S. Liu, H. Yu and P. Li, *ACS Appl. Mater.*, 2013, **5**, 598.
24 J. Wu, J. Wang, H. Li, Y. Du, K. Huang and B. Liu, *J. Mater. Chem. A*, 2013, **1**, 9837.
25 T. Hao, C. Yang, X. Rao, J. Wang, C. Niu and X. Su, *Appl. Surf. Sci.*, 2014, **292**, 174.
26 J. P. Dhal, B. G. Mishra and G. Hota, *Inter. J. Environ. Sci. Tech.*, 2015, **12**, 1845.
27 D. Maiti, S. Mukhopadhyay and P. S. Devi, *ACS Sustain. Chem. Eng.*, 2017, **5**, 11255.
28 S. K. Mohapatra, S. E. John, S. Banerjee and M. Misra, *Chem. Mater.*, 2009, **21**, 3048.
29 E. Asenath-Smith, R. Hovden, L. F. Kourkoutis and L. A. Estroff, *J. Am. Chem. Soc.*, 2015, **137**, 5184.
30 G. J. Hutchings, M. S. Hall, A. F. Carley, P. Landon, B. E. Solsona, C. J. Kiely, A. Herzing, M. Makkee, J. A. Moulijn, A. Overweg, J. C. Fierro-Gonzalez, J. Guzman and B. C. Gates, *J. Catal.*, 2006, **242**, 71.
31 E. Thimsen, F. Le Formal, M. Gratzel and S. C. Warren, *Nano. Lett.*, 2011, **11**, 35.
32 L. Han, Z. Shan, D. Chen, X. Yu, P. Yang, B. Tu and D. Zhao, *J. Colloid Interface Sci.*, 2008, **318**, 315.
33 L. Durães, B. F. O. Costa, J. Vasques, J. Campos and A. Portugal, *Mater. Lett.*, 2005, **59**, 859.
34 K. Fujii, T. Kumai, T. Takamuku, Y. Umebayashi, and S. Ishiguro, *J. Phys. Chem. A*, 2016, **110**, 1798-1804.
35 K. Nakanishi, *J. Porous Mater.*, 1997, **4**, 67.
36 D. M. Smith, D. Stein, J. M. Anderson and W. Ackerman, *J. Non-Cryst. Solids*, 1995, **186**, 104.

37 Flory. P. J., *J. Chem. Phys*., 1942, **10**, 51.
38 Huggins. M., *J. Phys. Chem*., 1942, **46**, 151.
39 Huggins. M., *J. Am. Chem. Soc*., 1942, **64**, 1712.

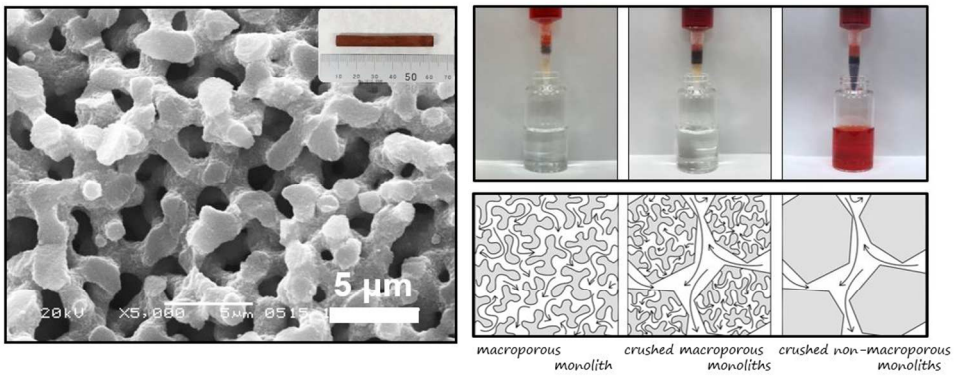

308x131mm (96 x 96 DPI)